Human ribosome interactions reframe neomycin toxicity

Xinyi Zhang[1,#], Lingfan Zhu[1,#], Changfeng Jia[1,#], Keqin Wu[1], Yuanjie Bai[1], Shuangli Sun[1], Zhe Zhang[1], Lei Guo[2], Xuben Hou[3]*, Meng Wu[1]*, Alexey Amunts[4,5,*], Wenfei Li[1,2,*]

1 School of Basic Medical Sciences, Cheeloo College of Medicine, Shandong University, Jinan, Shandong, China.

[2] Children's Hospital Affiliated to Shandong University, Jinan, Shandong, China

[3] Department of Medicinal Chemistry, Shandong Key Laboratory of Druggability Optimization and Evaluation for Lead Compounds, School of Pharmaceutical Sciences, Cheeloo College of Medicine, Shandong University, Jinan, Shandong, China.

[4] University of Münster, Schlossplatz 8, 48143 Münster, Germany

[5] Department of Structural Biochemistry, Max Planck Institute of Molecular Physiology, Otto-Hahn-Str. 11, 44227 Dortmund, Germany

[#] Equal contribution

[*] Correspondence to: wenfeili@sdu.edu.cn; alexey.amunts@gmail.com

Abstract

Aminoglycosides like neomycin are widely used but clinically limited due to toxicity, traditionally attributed to mitoribosome inhibition. Here, we demonstrate that this assumption requires re-evaluation by comparing neomycin's interactions with human ribosomes *in vitro* and in cells. While cryo-EM and biochemical assays reveal strong *in vitro* binding to both mitoribosomes and cytosolic ribosomes, especially at conserved regions such as the helix 44 (h44) decoding center despite sequence divergence, and H69. Cellular analyses show minimal impact on global translation, reduced occupancy on cytosolic ribosomes, and a complete absence of neomycin on mitoribosomes. These discrepancies suggest limited mitochondrial permeability rather than direct mitoribosome inhibition underlies neomycin's toxicity. Our findings redefine the mechanistic basis of aminoglycosides side effects and call for a reassessment of their cellular targets.

Introduction

Precise control of protein synthesis is fundamental to cellular life, and its disruption is a common target for antibiotics[1–4]. Although aminoglycosides are highly effective against bacteria, their systemic clinical use is constrained by significant oto- and nephrotoxicity in patients[5,6]. While selectivity of aminoglycosides for bacterial ribosomes is often attributed to structural variations within h44 decoding site compared to their eukaryotic counterparts[7,8], the structural similarity between bacterial and mitochondrial translation apparatus suggests a potential for off-target effects may underlie the observed human toxicities[9–15]. Aminoglycosides have been reported to interact with eukaryotic ribosomes, influencing translation fidelity or inducing premature termination codon readthrough[16–20]. Derivatives of aminoglycosides could further enhance specificity to eukaryotic ribosome for therapeutic purposes, such as leishmania targeting[21] or nonsense mutation suppression for genetic diseases[22].

Neomycin is a 4,5-linked aminoglycoside antibiotic[16,23] that inhibits bacterial translation primarily by binding to the decoding A site[24,25]. This involves binding to h44 of the small subunit (SSU) and H69 of the large subunit (LSU), thereby causing codon misreading and translation inhibition[3,24,26–28]. Molecular dynamics simulations of the decoding site showed that the catalytic activity also depends on rRNA A-site dynamics[29]. Despite the assumption that mitochondrial translation is the primary site of aminoglycoside toxicity, neomycin has also been shown to disrupt mitochondrial lipid metabolism, and promote pathological interactions with lipid droplets, leading to oxidative stress and impaired fatty acid utilization[30]. Thus, the understanding of neomycin's impact for guiding the development of safer therapeutic strategies warrants critical re-evaluation. A detailed investigation of neomycin's interaction with both human mitochondrial and cytosolic ribosomes is crucial for a complete picture of its cellular impact and for guiding the development of safer therapeutic strategies.

Previous studies successfully used addition of antibiotics streptomycin[31] and quinupristin/dalfopristin[32] directly to the cell culture to define their structures in the mitoribosome-bound form. In this study, we systematically investigate neomycin's action on mitoribosomes and cytosolic ribosomes from HEK (human embryonic kidney) 293-

60 derived cells. We determined the cryo-EM structures of human mitoribosomes and
61 cytosolic ribosomes bound to neomycin *in vitro*, then analyzed native ribosomes isolated
62 from drug-treated cells to assess neomycin's occupancy *in vivo.* Our results reveal
63 striking discrepancies between *in vitro* and *in vivo* drug behavior, including limited
64 engagement and selective loss of binding at key functional sites, such as h44, in the
65 cellular environment. These findings challenge the conventional views of neomycin's
66 mitochondrial toxicity and indicate that additional factors, including cellular bioavailability
67 barriers, redox-dependent binding plasticity, and ribosomal dynamics should be taken
68 into account when considering therapeutic strategies.

69

70 **Results**

71 **Distinct neomycin-binding landscape on human mitoribosome**

72 To investigate the molecular basis of neomycin's interaction with human mitoribosomes,
73 we performed cryo-EM on mitoribosomes rapidly isolated from HEK293F cells[33] and
74 incubated with 50 μM neomycin. This yielded six maps with nominal resolutions ranging
75 from 2.9−3.3 Å. These states were designated as "non-rotated A/A-P/P", "non-rotated
76 A/A-P/P-E/E", "partially rotated A/A-P/P-E/E", "partially rotated hybrid A/P-P/E", "rotated
77 empty", "rotated hybrid A/P-P/E" (**Supplementary Fig. 1, Supplementary Table 1**). The
78 map quality allowed us to consistently identify cofactors, including polyamines and Fe-S
79 clusters, associated with rRNA and proteins, in agreement with previous reports[15,31]
80 (**Supplementary Fig. 1c-d**). Neomycin composed of four linked monosaccharide rings
81 (I-IV), including a central 2-deoxystreptamine (ring II), and three amino-modified sugars
82 (**Fig. 1a**). Across the six states, we identified nine distinct densities corresponding to
83 neomycin molecules: three on the mitochondrial small ribosomal subunit (mtSSU) (Neo1-
84 3) and six on the mitochondrial large ribosomal subunit (mtLSU) (Neo4-9) (**Fig. 1b**,
85 **Supplementary Table 2**).

86 Specifically, Neo1 displayed well-defined density for all four rings (I-IV) and bound to h44
87 adjacent to the A-tRNA binding site within the decoding center (**Fig. 1c, Supplementary**
88 **Fig. 2**). This binding effectively blocks proper pairing of tRNA with mRNA, consistent with
89 observations in bacterial ribosomes[24,25] (**Supplementary Fig. 3a**). Neo1 establishes

90 potential hydrogen bonds with several nucleotides from the mtSSU including G1489,
91 U1490, C1491, A1555, A1557, A1558, G1559 and U1560 (**Fig. 1c, Supplementary Fig.**
92 **2d**). Notably, ring I of Neo1 forms stable π-π stacking with the nucleobase C1556 (**Fig.**
93 **1c, Supplementary Fig. 2d**). Furthermore, two conserved nucleotides, A1447 and A1558
94 (equivalent to A1492/A1493 in bacteria), are observed to flip out of h44 (**Fig. 1c**), a
95 characteristic of sampling the codon-anticodon interaction that facilitates near cognate
96 tRNA incorporation of incorrect amino acid during protein synthesis[34–36].

97 The Neo2 molecule, situated in a pocket formed by h1 and h44, displayed well-identified
98 density for all four rings (**Fig. 1d, Supplementary Fig. 3c**). It establishes potential
99 hydrogen bonds with the nucleobase of C1481 and sugar-phosphate backbone of U656,
100 G657, G658 and G899 from the mtSSU (**Fig. 1d**). Similarly, the Neo3 molecule binds to
101 h28 near the P-tRNA, stabilized by hydrogen bonds with nucleotides from the mtSSU
102 (specifically, the phosphate group of G1469 and A1470; and the nucleobases from G1472,
103 C1473, G1474, G1178, U1180 and C1182 (**Fig. 1e, Supplementary Fig. 3c**). Neo4 binds
104 to the terminal hairpin of H69, stabilized by nucleotides from both the mtSSU (G1079
105 U1081 and G1582) and mtLSU (C2583 and U2586) (**Fig. 1f, Supplementary Fig. 2e,**
106 **Supplementary Fig. 3c**). H69 is recognized as another critical binding pocket for
107 aminoglycosides. Consistent with previous bacterial structural data[24,25], Neo1 and Neo4
108 represent conserved neomycin binding sites in human mitoribosomes, located within the
109 h44 and H69 regions, respectively (**Supplementary Fig. 3a-b**).

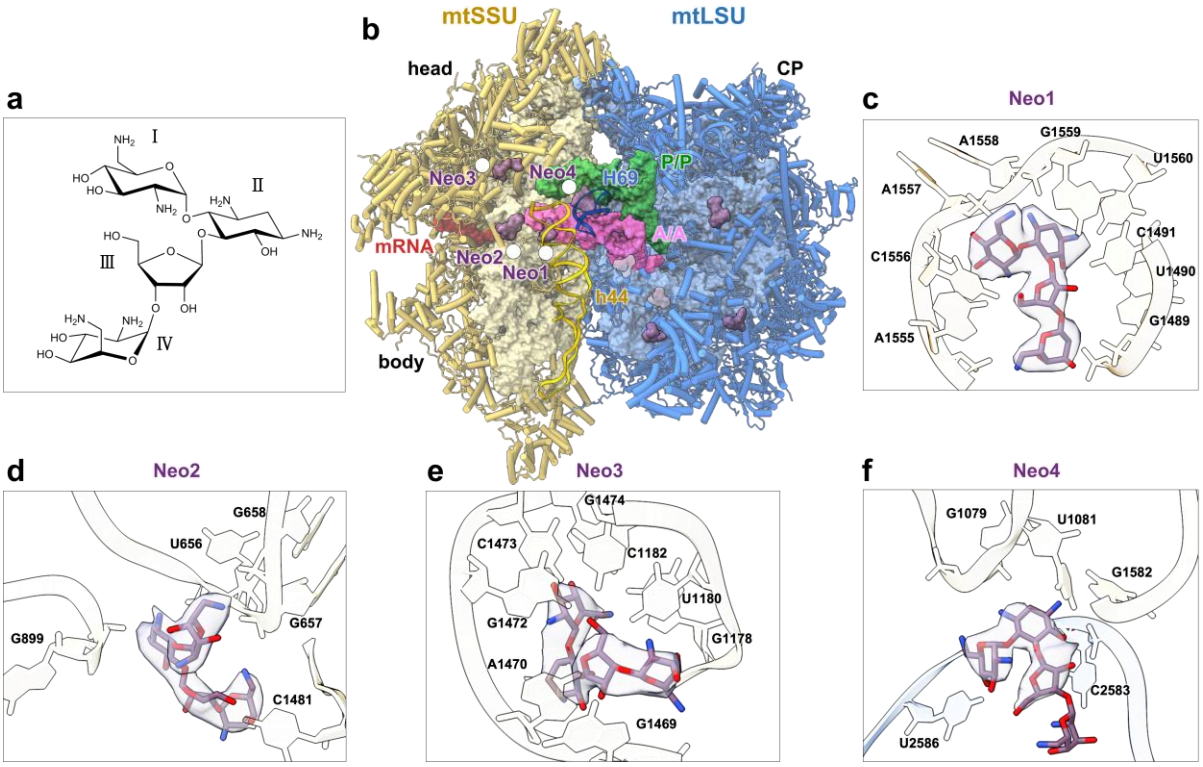

Fig. 1| Structural analysis of neomycin binding to mitoribosome *in vitro*. a Chemical structure of neomycin. **b** Overall structure of the neomycin-bound mitoribosome in non-rotated state comprising the mtSSU (yellow), mtLSU (blue), mRNA (red), A-site tRNA (magenta) and P-site tRNA (green). rRNA helices h44 and H69 are shown as cartoon in gold and blue, respectively. **c** Close-up view of Neo1 occupying the conserved pocket formed by h44. **d** Close-up view of Neo2 binding pocket formed by residues from h1 and h44. **e** Close-up view of Neo3 binding pocket in h28. **f** Close-up view of Neo4 binding pocket formed by H69 and stabilized by both H69 and nucleotides from the mtSSU. Key interacting nucleotides are represented as sticks (oxygen in red, nitrogen in blue).

The engagement of neomycin, particularly h44 and H69, was found to be dependent on the rotational state of the mitoribosome (**Supplementary Table 2**). Specifically, Neo1 binds to h44, exhibited well-defined density for all four of its rings across various non-rotated and partially rotated states (**Supplementary Table 2**). However, it was notably absent in the functional rotated state containing A/P and P/E tRNAs (**Supplementary Table 2**). This suggests that neomycin binding to h44 preferentially stabilizes non-rotated

127 or partially rotated conformations, thereby preventing the mitoribosome from fully entering
128 the functional rotated state. This observation aligns with findings in bacterial systems,
129 where neomycin binding to h44 is known to restrict subunit rotation and maintain a non-
130 rotated state, providing a structural basis for its inhibitory mechanism[24,27].

131 For H69, discernible densities for rings I to III of neomycin were observed in both rotated
132 and non-rotated states only when tRNAs occupied the A and P sites (**Fig. 1f,**
133 **Supplementary Table 2**). Intriguingly, H69 binding was absent in partially rotated states
134 (**Supplementary Table 2**). This indicates that H69 binding is contingent upon specific
135 tRNA occupancy and ribosomal conformation, favoring either the non-rotated or fully
136 rotated states with engaged tRNAs. Collectively, this conformational state-dependent
137 binding of neomycin to both h44 and H69 on the mitoribosome suggests a dynamic
138 interplay between drug association and the ribosome's structural landscape, paralleling
139 similar mechanisms observed in bacterial ribosomes.

140

141 **Structural analysis reveals canonical and novel neomycin-binding sites on the**
142 **human cytosolic ribosome**

143 To understand the impact of neomycin on human cellular translation and its potential
144 toxicity, we assessed its interaction with human cytosolic ribosomes (**Supplementary Fig.**
145 **4, Supplementary Table 3**). While previous studies have indicated sequence differences
146 in the critical h44 region of human ribosomes compared to their bacterial counterparts
147 (**Supplementary Fig. 2a-c**), potentially affecting aminoglycoside binding[3,24,26–28], our *in*
148 *vitro* translation (IVT) assays revealed that neomycin significantly inhibits cytosolic
149 ribosomes activity, with a half-maximal inhibitory concentration (IC_{50}) of approximately 50
150 μM (**Fig. 2a**). This finding suggests that neomycin can effectively target human cytosolic
151 ribosomes and inhibit its translation.

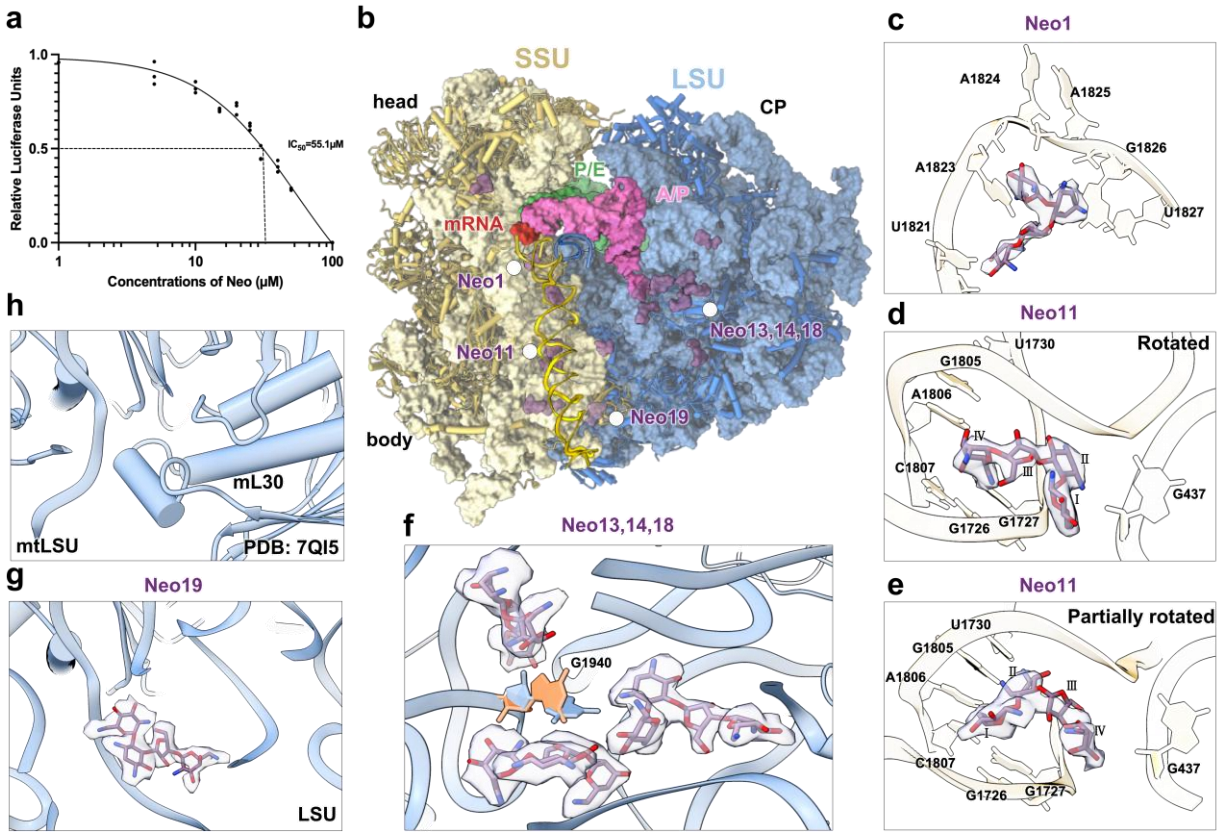

Fig. 2| Structural analysis of neomycin binding to cytosolic ribosomes *in vitro*. a Luciferase reporter assays of cytosolic ribosomes in response to neomycin at different concentrations of 1, 5, 10, 15, 20, 25, 30, 40, 50 and 100 μM (data present mean ± s.d., n = 3 independent experiments). **b** Overall structure of neomycin-bound cytosolic ribosomes in rotated state comprising the SSU (yellow), LSU (blue), mRNA (red), A/P-site tRNA (magenta) and P/E-site tRNA (green). rRNA helices h44 and H69 are shown as cartoon in gold and blue respectively. **c** Close-up view of Neo1 bound to h44. **d** Close-up view of Neo11 bound to a novel pocket within h44 in the rotated state. **e** A different conformation of Neo11 bound to in the partially rotated state. **f** A novel pocket accommodating three neomycin molecules (Neo13, Neo14, and Neo18), with G1940 adopting a unique conformation upon neomycin binding (orange represents the conformation before binding, blue represents the conformation after binding). **g** Close-up view of Neo19 bound to a pocket formed by H53 and H54 from the LSU. **h** Comparison showing that in the mitoribosome, the Neo19 site is preoccupied by mitochondrial protein mL30 (PDB: 7QI5[15]).

169 To further elucidate the molecular mechanism of this inhibition and the specific binding
170 modes of neomycin on the cytosolic ribosome, we subsequently performed cryo-EM
171 analysis of cytosolic ribosome complexes incubated with 50 μM neomycin (**Fig. 2**,
172 **Supplementary Fig. 4, Supplementary Table 3**). Our single-particle analysis yielded
173 structures of ribosomes in three distinct translational states: non-rotated, partially rotated
174 and rotated (**Supplementary Fig. 4a**). Across these maps, we identified neomycin
175 molecules bound at 17 distinct pockets: three on the small ribosomal subunit (SSU) (Neo1,
176 Neo10 and Neo11) and fourteen on the large ribosomal subunit (LSU) (Neo12-Neo25)
177 (**Fig. 2b, Supplementary Table 4**). Notably, the majority of these binding pockets were
178 consistently occupied by neomycin across the different ribosomal states (**Supplementary**
179 **Table 4**).

180 A well-established mechanism for aminoglycoside action in bacteria involves binding to
181 the decoding center, primarily formed by h44 of the small subunit[3,24,26–28]. We observed
182 analogous binding in the human cytosolic ribosome despite sequence differences (**Fig. 2,**
183 **Supplementary Fig. 2a-c**). Our structures of the neomycin-bound human cytosolic
184 ribosome revealed Neo1 at the universally conserved aminoglycoside binding pocket
185 within h44 (**Fig. 2b-c, Supplementary Table 4**). While the overall binding mode is
186 conserved, superimposition of human and bacterial h44 structures indicated slight
187 conformational changes and subtle differences in the precise neomycin binding pose
188 (**Supplementary Fig. 5a-c**). Neo1 interacts with U1821-U1827 of h44, with A1824 and
189 A1825 (equivalent to A1492/A1493 in bacteria) flipped out from the helix, consistent with
190 observations in bacteria and mitoribosomes (**Fig. 1c, Fig. 2c**).

191 Intriguingly, we also identified a second neomycin molecule (Neo11) bound to a novel,
192 distinct pocket located centrally on h44, away from the canonical A-site tRNA binding
193 region (**Fig. 2d-e**). The conformation of Neo11 within this pocket exhibited significant
194 differences between the partially rotated and rotated states (**Fig. 2d-e**). Specifically, in
195 the rotated ribosome, ring I of Neo11 directly interacts with G437 from the SSU via a
196 hydrogen bond, while ring IV forms hydrogen bonds with h44 residues, including G1726,
197 G1727 and A1806 (**Fig. 2d**). In contrast, in the partially rotated state (characterized by an
198 approximate 5° rotation of the SSU relative to the one from the rotated state), this pocket
199 undergoes a spatial displacement of approximately 3 Å. Meanwhile, Neo11 undergoes a

200 180° flip with its ring I approaching the A1806 direction (**Fig. 2e**). This conformational
201 rearrangement leads to entirely distinct interactions between Neo11 and h44: ring I forms
202 a hydrogen bond with C1807, ring II interacts with U1730 and G1805 (proximal of A1806),
203 and ring IV engages with the phosphate group of G1726 and G1727 (**Fig. 2e**). These
204 latter interactions, where nucleobases stabilize neomycin, occur specifically in the rotated
205 state. These dynamic binding characteristics suggest a potential link between the novel
206 Neo11 binding site and ribosome dynamics. Notably, unlike in bacterial ribosomes and
207 mitoribosomes where H69 is a conserved aminoglycoside pocket, no neomycin binding
208 was observed to H69 of the human cytosolic ribosome, likely due to sequence differences
209 in human H69 causing a relatively smaller pocket and potential steric clash
210 (**Supplementary Fig. 5d**).

211 Beyond these h44-proximal sites, we identified a large, previously uncharacterized pocket,
212 formed by helices H89 and H72 of the LSU rRNA and a conserved rRNA loop (C1928-
213 C2053) (**Fig. 2f**). This pocket simultaneously accommodates three neomycin molecules
214 (Neo13, Neo14, and Neo18) (**Fig. 2f**). Upon neomycin binding within this pocket, we
215 observed a distinct conformational change in nucleotide G1940 (**Fig. 2f**). This specific
216 conformational alteration of G1940 was consistently present across all structural classes
217 of neomycin-bound ribosomes. Analyzing the identified binding pockets revealed
218 significant differences compared to those observed in mitoribosomes, with the exception
219 of the universally conserved Neo1 site (**Supplementary Tables 2 and 4**). Several
220 neomycin-binding pockets appeared to be specific to the human cytosolic ribosome,
221 occupying regions that correspond to different ribosomal proteins in the bacterial
222 ribosome or mitoribosome (**Fig. 2g-h, Supplementary Fig. 5e-g**). For example, Neo19
223 binds to a pocket formed by LSU nucleotides, a pocket absents in mitoribosomes as it is
224 occupied by the mL30 protein (**Fig. 2g-h**). These differences highlight the distinct
225 structural landscapes of various ribosomes. Collectively, these multiple binding
226 interactions, particularly at the h44 decoding center, provide a structural rationale for the
227 neomycin-induced inhibition of cytosolic translation observed in our IVT assays (**Fig. 2**).

228

229 **Absence of neomycin binding to mitoribosomes in cells**

While our cryo-EM data analysis revealed multiple binding of neomycin to both mitoribosomes and cytosolic ribosomes *in vitro* (**Figs. 1 and 2**), its effects on cellular translation were mild. Cell viability assays (CCK8) indicated limited cytotoxicity upon short-term neomycin exposure with an IC_{50} of approximately 1.2 mM after prolonged (72 h) treatment (**Fig. 3a**). Consistent with this, L-azidohomoalanine (L-AHA) labeling assay (a method for detecting newly synthesized nascent chains)[37–39] showed no significant change of global mitochondrial translation (**Fig. 3b**).

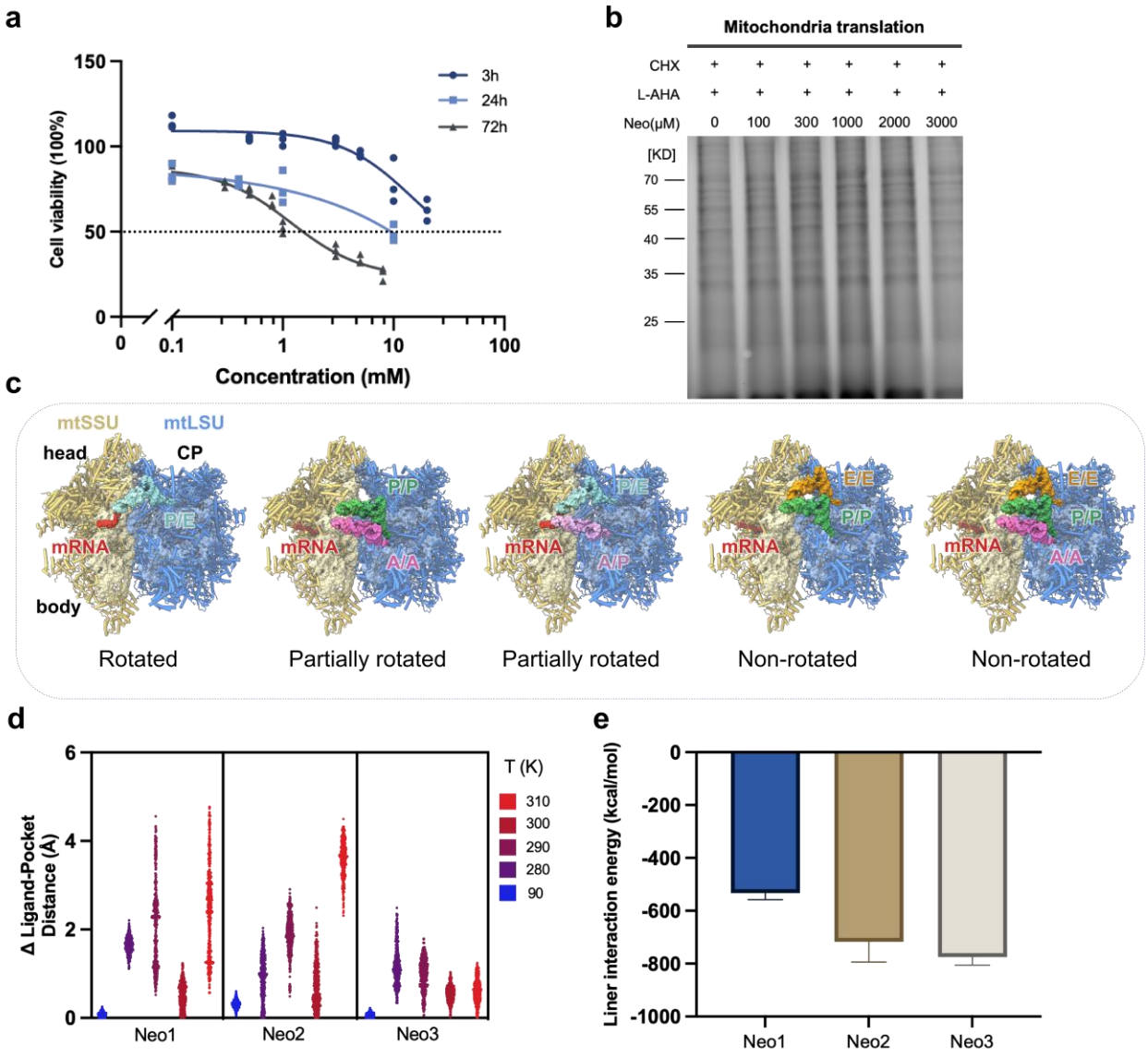

Fig. 3| *In vivo* effects and structural dynamics of neomycin on human mitoribosomes. **a** Cell viability of HEK293T cells measured by the CCK-8 assay after

241 treatment with increasing concentrations of neomycin for 3 h, 24 h, and 72 h respectively
242 (data present mean ± s.d., n = 3 independent experiments). **b** *De novo* mitochondrial
243 nascent protein synthesis measured via L-AHA labeling. **c** Overall cryo-EM structure of
244 native mitoribosome with different tRNAs and cofactors. Coloring is consistent with
245 previous figures. **d** MD simulations depicting the temperature-dependent binding stability
246 of neomycin molecules (Neo1, Neo2, and Neo3) within the mtSSU, illustrating the relative
247 movement of the neomycin molecules within their binding pocket. The changes in
248 distance between the ligand mass center and the binding pocket mass center (defined as
249 the centroid of residues within 3 Å of the ligand in initial cryo-EM structure) during
250 molecular dynamics simulations at temperatures ranging from 90 K to 310 K. **e** Calculated
251 linear interaction energy for neomycin within the mtSSU.
252

253 To investigate this discrepancy between *in vitro* potency and *in vivo* cellular effects, we
254 conducted comprehensive structural, biochemical and computational analysis of the
255 native ribosome (**Supplementary Figs. 6-10**). We isolated the native translation
256 complexes from the kidney-derived HEK293F cells treated with 1 mM neomycin. This
257 concentration, while higher than typical plasma levels (up to ~0.13 mM), is clinically
258 relevant as neomycin accumulates to millimolar concentrations in the kidney—a primary
259 site of its toxicity[40,41]. As previously shown[31,42,43] this approach implies that the
260 antimicrobial would have to be imported into mitochondria, preserving more native states.
261 Mitoribosomes were then isolated and subjected to a cryo-EM analysis (**Supplementary**
262 **Fig 6, Supplementary Table 5**).

263 The cryo-EM analysis of mitoribosomes from treated cells yielded six distinct translational
264 states characterized by varying SSU rotations and associated translation factors (**Fig. 3c,**
265 **Supplementary Fig. 6**). Consistent with our biochemical data showing limited cellular
266 toxicity and effect on mitochondrial translation upon neomycin treatment (**Fig. 3a-b**), our
267 structural analysis revealed a striking absence of bound neomycin molecules on human
268 mitoribosomes isolated from these treated cells (**Fig. 3c, Supplementary Table 2**). This
269 indicates that under the cellular conditions, neomycin does not stably associate with or
270 significantly inhibit human mitoribosomes *in vivo*.

271 At physiological temperatures, biomolecules can access a broader range of
272 conformations, and the rates of conformational switching are generally faster than at
273 lower temperatures[44]. Although rapid cooling during cryo-EM sample preparation can
274 kinetically trap molecules in states representative of the room-temperature ensemble[3,44].
275 It remains crucial to assess if the binding pocket for neomycin adopts a non-binding-
276 competent conformation specifically at physiological cellular temperatures *in vivo*. To
277 investigate this, we performed all-atom explicit-solvent molecular dynamics (MD)
278 simulations of the mtSSU with bound neomycin, focusing on the decoding center (**Fig.
279 3d-e, Supplementary Fig. 9**). Molecular dynamics (MD) simulations were initiated from
280 the cryo-EM structure and performed across a range of temperatures up to physiological
281 conditions. For each temperature, five independent replicates were conducted,
282 accumulating a total simulation time of 0.5 μs. As anticipated, the fluctuation of the
283 antibiotic's atomic positions, quantified by root mean square deviation (RMSD) analysis,
284 increased with rising temperature (**Supplementary Fig. 9b**). Despite these thermal
285 fluctuations, the neomycin molecules remained stably associated with their binding sites
286 within the mitoribosome, and the average conformations of the bound drugs were
287 consistent with those observed in the cryo-EM structure (**Fig. 3d**). The consistent
288 association of neomycin with its mitoribosomal binding sites even at physiological
289 temperatures effectively rules out temperature-driven conformational changes as the sole
290 reason for its observed absence *in vitro*. Furthermore, comparative analysis of the MD
291 trajectories revealed enhanced binding stability of neomycin at the Neo1 site relative to
292 Neo2 and Neo3, evidenced by lower ligand RMSD values and reduced calculated linear
293 interaction energy (**Fig. 3e**).

294

295 **Reduced engagement of neomycin with human cytosolic ribosomes *in vivo***

296 Despite strong *in vitro* inhibition of cytosolic ribosomes and observed binding to the key
297 h44 site in *in vitro* incubated structures (**Fig. 2**), neomycin treatment did not markedly
298 inhibit nanoluciferase expression in cells, even at high concentrations (**Fig. 4a,
299 Supplementary Fig. 8a and c**). This suggests a limited overall effect on cellular
300 translation. Although L-AHA labeling assay showed no significant change of global

301 cytosolic translation, we did observe an increase in stop codon readthrough in a reporter
302 cell line upon neomycin treatment (**Fig. 4b-c, Supplementary Fig. 8b**). This suggests
303 that neomycin can influence cytosolic translation fidelity, even with minimal overall
304 inhibition. To further understand neomycin's cellular effect on cytosolic translation, we
305 isolated cytosolic ribosomes from the same batch of neomycin-treated cells used for
306 mitoribosome analysis. Our analysis revealed ribosomes in four different states, with the
307 rotated state being the most prevalent (**Supplementary Fig. 7, Supplementary Table**
308 **5**). We detected 15 neomycin molecules bound to the ribosomes, occupying some of the
309 same pockets identified in our *in vitro* incubation experiments (**Supplementary Table 4**).
310 Notably, densities for some sites such as Neo21 and Neo19 were diminished or absent
311 in the cellular samples compared to the *in vitro* incubated ribosomes (**Supplementary**
312 **Table 4**). Strikingly, the Neo1 site within the canonical h44 decoding center, a key binding
313 site *in vitro*, was completely devoid of neomycin in the cellular dataset (**Supplementary**
314 **Table 4, Fig. 4d**). This absence occurred despite no significant conformational changes
315 in the h44 pocket or novel post-translational modifications in the decoding center
316 (**Supplementary Fig. 8e**). We performed temperature-dependent MD simulations on the
317 SSU was conducted for the SSU with its bound neomycin molecules, including Neo1.
318 Although the neomycin molecules and their binding pocket displayed conformational
319 change with increasing temperatures (**Supplementary Fig 9d and f**), their binding
320 relative to their pockets remained stable with minor RMSD during simulations (**Fig. 4e**),
321 excluding temperature-driven conformational changes as the sole cause for its *in vitro*
322 absence. Additionally, neomycin binding at Neo1 site exhibited significantly stronger
323 affinity than at Neo10 or Neo11 from the SSU, evidenced by much lower interaction
324 energies (**Fig. 4f**), indicating that the lack of h44 bound neomycin is not due to weak
325 binding affinity.

326 Our *in vivo* structural findings, particularly the reduced occupancy on cytosolic ribosomes
327 (**Supplementary Table 4**), suggest that the cellular environment critically modulates
328 neomycin's interactions, contrasting with direct incubation experiments. One notable
329 difference is the cellular redox state, maintained by glutathione (GSH), which is altered
330 upon cell lysis for *in vitro* studies. Our *in vitro* translation assays showed that the reducing
331 agent TCEP or GSH provided a protective effect against neomycin's inhibitory action at

certain concentrations (**Fig. 4g, Supplementary Fig. 8d**), consistent with research that GSH can reduce neomycin toxicity[45,46]. This suggests that the reducing intracellular environment may diminish its binding for this site *in vivo* (**Supplementary Table 4**). Moreover, at higher concentrations (3 mM) and prolonged exposure, neomycin binding became restricted to only two pockets (**Supplementary Tables 4-5, Supplementary Fig. 10**), suggesting that cellular mechanisms, such as drug efflux, may actively limit neomycin's interaction with its targets.

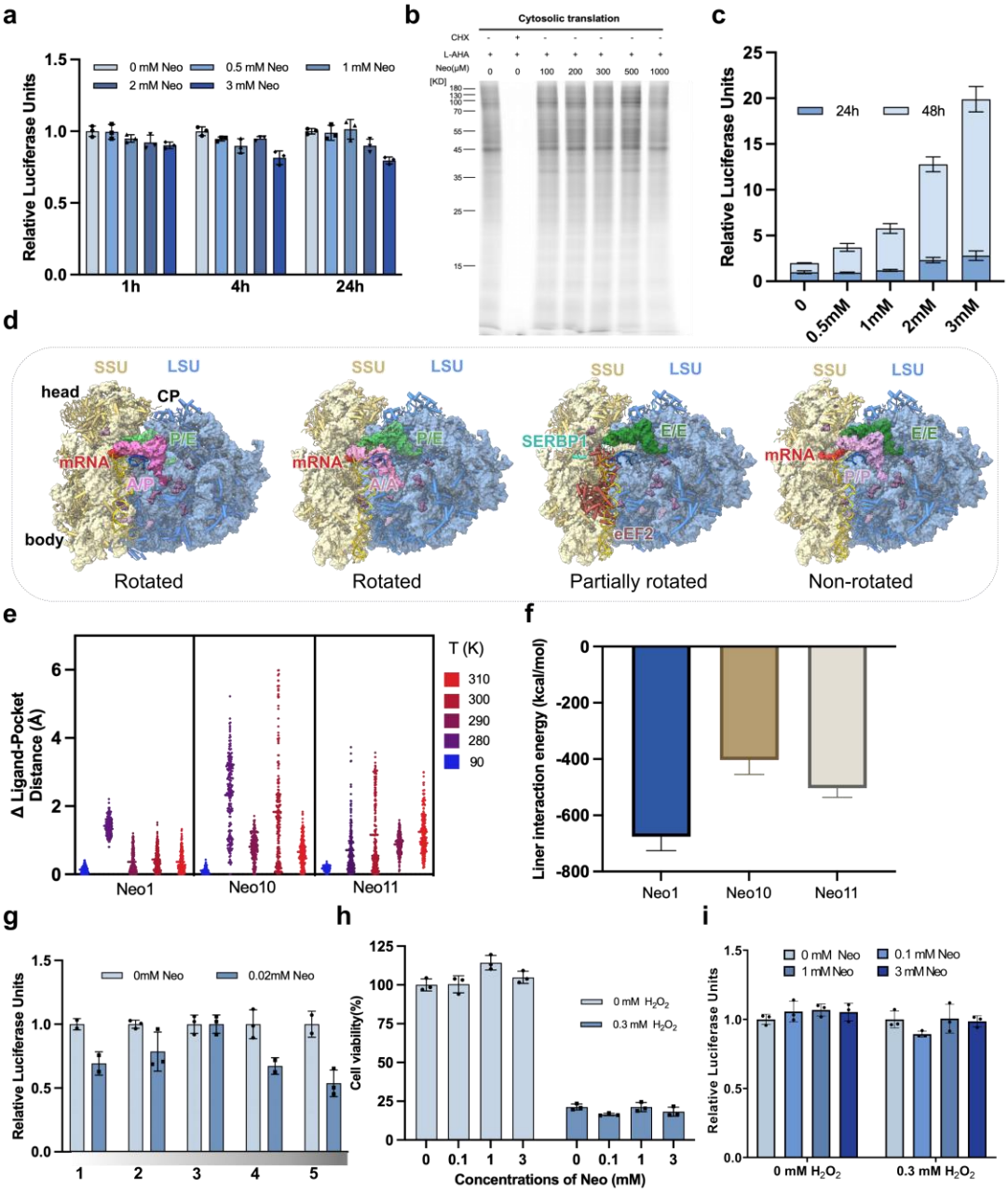

340 **Fig. 4| *In vivo* effects and structural analysis of neomycin with human cytosolic**
341 **ribosomes. a** *In vivo* translation assays using the NLuc cell line at various time points
342 following treatment with different concentrations of neomycin (data present mean ± s.d.,
343 n = 3 independent experiments). **b** *De novo* nascent protein synthesis measured via L-
344 AHA labeling. **c** Quantification of CFTR nonsense allele readthrough in cultured HEK293T
345 cells treated with increasing concentrations of neomycin for 24 h and 48 h (data present
346 mean ± s.d., n = 3 independent experiments). **d** Overall cryo-EM structure of native
347 cytosolic ribosomes with different tRNAs and cofactors. Coloring is consistent with
348 previous figures. **e** MD simulations depicting the temperature-dependent binding stability
349 of neomycin molecules (Neo1, Neo10, and Neo11) within the SSU, illustrating the relative
350 movement of the neomycin molecules within their binding pocket. The changes in
351 distance between the ligand mass center and the binding pocket mass center (defined as
352 the centroid of residues within 3 Å of the ligand in initial cryo-EM structure) during
353 molecular dynamics simulations at temperatures ranging from 90 K to 310 K. **f** Calculated
354 linear interaction energy for neomycin within the SSU. **g** *In vitro* translation assays with
355 luciferase reporters in the presence of 0.02 mM neomycin under varying redox conditions
356 (data present mean ± s.d., n = 3 independent experiments). The grey bar indicates an
357 increasingly reducing environment, established by increasing concentrations of TCEP
358 (lane 1: 0.1 mM H_2O_2; lane 2: 0 mM TCEP; lane 3: 0.1 mM TCEP; lane 4: 1 mM TCEP;
359 lane 5: 5 mM TCEP). **h** Cell viability of HEK293T cells measured by the CCK-8 assay
360 after treatment with increasing concentrations of neomycin in the presence or absence of
361 H_2O_2 (data present mean ± s.d., n = 3 independent experiments). **i** *In vivo* translation
362 assays with luciferase reporters in response to different concentrations of neomycin in a
363 0.3 mM H_2O_2 environment (data present mean ± s.d., n = 3 independent experiments).
364

365 **Discussion**

366 This study provides insights into neomycin's interaction with human ribosomes by
367 uncovering the differences between its *in vitro* binding properties and in-cell behavior. We
368 show that neomycin's activity is modulated by the cellular environment, which can
369 diminish or prevent its engagement with key ribosomal targets. Our findings highlight a
370 clear divergence between *in vitro* and *in vivo* neomycin-ribosome interactions. *In vitro*,

371 neomycin robustly binds conserved sites on both mitoribosomes and cytosolic ribosomes,
372 including the bacterial-like decoding center at h44 (**Figs. 1-2, Supplementary Tables 2**
373 **and 4**). Crucially, however, in cells neomycin fails to occupy these sites, most notably
374 h44 in cytosolic ribosomes, and is undetectable on mitoribosomes (**Fig. 3-4**,
375 **Supplementary Table 2**). These observations correlate with minimal inhibition of global
376 translation, suggesting intracellular factors, such as limited mitochondrial permeability
377 and redox balance may restrict neomycin's effective access. We propose that the cellular
378 reducing environment alters neomycin's binding affinity, a hypothesis supported by
379 translation assays showing redox-dependent modulation of neomycin activity (**Fig. 4**,
380 **Supplementary Fig. 8**). Moreover, restricted engagement at higher drug concentrations
381 implies additional resistance mechanisms, further limiting neomycin's impact. Beyond
382 direct ribosomal inhibition, other potential toxicity mechanisms exist, as exemplified by a
383 recent finding that neomycin induces toxicity by mediating PGC-1α imbalance of
384 mitochondria-lipid droplet homeostasis[30].

385 Expanding on these insights into cellular accessibility, our observations reveal that
386 neomycin binds the decoding center (h44 and H69) in a ribosomal state-dependent
387 manner. This suggests that its interactions with both mitoribosomes and cytosolic
388 ribosomes are influenced by subunit rotation, aligning with the known mechanism by
389 which 4,5-linked aminoglycosides antibiotics stabilize the non-rotated state and thereby
390 inhibit translocation[24,27]. Furthermore, while the binding of neomycin to mitoribosomes
391 and cytosolic ribosomes differs overall, except for Neo1 in the canonical h44 pocket, the
392 fundamental contact modules of neomycin remain conserved. To investigate this in detail,
393 we quantified the interacting frequency of each neomycin atom across previously reported
394 bacterial ribosome structures and human ribosome structures (mitoribosome and
395 cytosolic ribosome) determined in our study. Our analysis revealed that, consistent with
396 prior bacterial studies, rings I and II of neomycin are the most frequently utilized moieties
397 for ribosomal interaction[24,27], playing a crucial role in neomycin's binding (**Supplementary**
398 **Fig. 9g-i**). Specifically, these two -NH_2 groups from ring II (2-DOS ring, the core of
399 aminoglycosides) exhibit the highest frequency of interactions across all three ribosome
400 types, closely followed by the -OH and 6'-NH_2 groups from ring I (**Supplementary Fig.**
401 **9g-i**). The strong binding capabilities of these amino groups stem from their ability to form

402 hydrogen bonds with phosphate oxygen atoms within the ribosome's rRNA backbone or
403 with nucleotide hydroxyl groups. Furthermore, their typical positive charge enables robust
404 electrostatic interactions with the negatively charged phosphate backbone of the
405 ribosome.

406 Collectively, our study demonstrates that neomycin-ribosome interactions are not static
407 but highly sensitive to various factors like the ribosomal state and cellular redox
408 environment, indicating an additional level of complexity in the ribosome-antibiotic binding
409 studies. Moreover, our findings challenge the prevailing assumption that mitochondrial
410 translation inhibition is the primary cause of neomycin toxicity, as neomycin was notably
411 absent on native mitoribosomes *in vivo*. Instead, toxicity may involve metabolic
412 disturbances or drug accumulation under pathological conditions. The resilience of
413 mitoribosomes to neomycin may also arise from an adaptive cellular response, inherent
414 insensitivity to certain threshold levels, or a limited import into mitochondria. However, the
415 specific mechanistic processes essential for neomycin binding warrant further
416 investigation. In the future, the structural studies of native samples will help to better
417 understand the related pathological dysfunctions.

418

419 **Methods**

420 **Cell lines and cell culture**

421 HEK293T cells were cultured at 37 °C and 5% CO_2 in Dulbecco's Modified Eagle's
422 Medium (DMEM, Gibco, C11995500BT) supplemented with 10% fetal bovine serum (FBS,
423 Excell Bio, FSP500). HEK293F cells were cultured in SMM 293-TII expression medium
424 (Sino Bio, M293TII) in shake flasks at 37 °C, 5% CO_2 and 110 rpm.

425

426 **Plasmid construction and generation of stable cell lines**

427 Clonal stable cell lines expressing NanoLuciferase (NLuc) or Cystic Fibrosis
428 Transmembrane Conductance Regulator (CFTR) were generated as previously
429 described[47]. The NLuc expression construct was generated by PCR amplification of
430 NLuc-Flag fragments, subsequently assembled into a linearized vector (originally derived

431 from Jamie H. D. Cate's laboratory) via Gibson Assembly. For the *CFTR* plasmid, *CFTR-*
432 *G542X (UGA)* along with the G542X context (seven codons upstream and downstream)
433 was fused to mEGFP and NLuc. This recombinant fragment was cloned into the same
434 laboratory-derived backbone vector using Gibson Assembly. The CFTR-G542X mutant
435 was created through site-directed mutagenesis of wild-type *CFTR* cDNA templates. The
436 plasmid construct was subsequently transfected into HEK293T cells and stable
437 transfectants were selected using 1 μg/ml puromycin for two weeks.

438

439 ***In vivo* translation assays**

440 The effect of neomycin on cytosolic translation was evaluated using the NLuc cell lines,
441 which were exposed to different concentrations of neomycin (0.5, 1, 2 and 3 mM) or
442 DMEM as a control. Luciferase activity was quantified after 1, 4, and 24 h using microplate
443 luminometer (BERTHOLD, Centro XS3 LB 960). To access the impact of the redox
444 environment on neomycin toxicity, 0.3mM H_2O_2 was co-administered with varying
445 concentrations of neomycin (0.1, 1, and 3 mM) for 1 h. Additionally, to determine the
446 readthrough effect of neomycin, the CFTR cell lines were treated with different
447 concentrations of neomycin (0.5, 1, 2, and 3 mM) for 24 h and 48 h respectively.

448

449 ***In vitro* transcription and translation assays**

450 The DNA template for *in vitro* transcription was PCR-amplified from plasmid pGM_EMCV-
451 NLuc using primers encoding T7 RNA polymerase promoter and poly-A tail sequences.
452 The *in vitro* transcription reaction was performed as previously described[47]. mRNA
453 transcripts were assessed for quality and size by gel electrophoresis, quantified
454 spectrophotometrically (Implen spectrophotometer, Nanophotometer NP80), diluted to 1
455 μg/μL, aliquoted, and preserved at -80 °C prior to *in vitro* translation reactions.

456 HEK293T cells were harvested at ~80% confluency and resuspended in ice-cold lysis
457 buffer (10 mM HEPES-KOH pH 7.5, 10 mM KOAc, 0.5 mM $Mg(OAc)_2$, 5 mM DTT) at a
458 1:1 (v/v) ratio. The HEK293T cell lysates and IVT reaction systems were prepared as
459 described previously[48,49]. Neomycin (MCE, HY-17624A) was introduced at different

460 concentrations as experimental variables in the reaction system at final concentrations of
461 1 μM, 5 μM, 10 μM, 15 μM, 25 μM, 30 μM, 40 μM, 50 μM and 100 μM. Reactions were
462 equilibrated at 30 °C for 25 min prior to luciferase activity measurement using a microplate
463 luminometer (BERTHOLD, Centro XS3 LB 960). Lysates and mRNA aliquots from
464 identical preparation lots were used for comparative assays within individual experimental
465 series to control batch variability.

466

467 **Cell counting kit-8 (CCK-8) cell growth assay**

468 The cytotoxicity of neomycin was measured in HEK293T cell lines using the CCK-8 assay.
469 Approximately 8000 cells per well were seeded in a 96-well plate in DMEM medium
470 supplemented with 10% FBS. After 24 h of adhesion, the cells were treated with different
471 concentrations of neomycin dilutions versus DMEM vehicle control. After 72 h of
472 incubation, culture medium was replaced with fresh DMEM medium supplemented with
473 CCK-8 (10% v/v reagent: medium ratio) for an additional 2 h of light-protected incubation.
474 Cellular viability was determined by measuring at 450 nm using a microplate reader. The
475 cytotoxic concentration that inhibits 50% viability (IC_{50}) of neomycin was calculated by
476 fitting the dose-response curve using GraphPad Prism software. All experiments were
477 performed in biological triplicates (n = 3).

478

479 **L-AHA labeling of nascent polypeptides**

480 L-AHA labeling of mitochondrial-encoded nascent polypeptides was performed as
481 described previously[39]. Briefly, the cells were treated with different concentrations of
482 neomycin and 50 μg/mL cycloheximide (CHX, MCE, HY-12320), which selectively inhibits
483 eukaryotic cytosolic ribosome activity by blocking translational elongation. Fluorescence
484 signals were analyzed using an Amersham Typhoon 5 (Cytiva).

485 For the cytosolic nascent polypeptide labeling, the procedure mirrored that used for
486 mitochondrial-encoded nascent polypeptides, with cells treated with 50 μg/mL CHX as a
487 positive control. Following the labeling, cells were harvested and resuspended in buffer
488 containing 60 mM Tris-HCl pH 8.0, 50 mM NaCl, 2 mM $MgCl_2$, 40 mM KCl, 5% glycerol,

489 0.1% NP-40 and 1× protease inhibitor and were subsequently homogenized on ice using
490 a glass dounce homogenizer. The resulting cell lysate was cleared by centrifugation at
491 15,000 ×*g* for 15 min at 4 °C, and the supernatant was transferred to new 1.5 mL tubes.
492 The click reaction and the following protein signal detection were performed as described
493 above. All experiments were performed in triplicate (n = 3 independent experiments).

494

495 **Isolation of mitochondria and purification of mitoribosomes**

496 Mitochondria isolation was performed as described previously[42]. A final volume of 1L
497 HEK293F cells at a density of 3×10^6 cells/ml was harvested, washed with Phosphate
498 Buffered Saline (PBS) buffer, and resuspended in 60mL mitochondrial isolation buffer (50
499 mM HEPES-KOH pH 7.5, 10 mM KCl, 1.5 mM $MgCl_2$, 1 mM EDTA, 1 mM EGTA, 1 mM
500 DTT, protease inhibitors). Cells were lysed by grinding in a glass dounce homogenizer
501 and lysate was clarified by centrifugation at 1000 ×*g* for 15 min, then 10,000 ×*g* for 15min
502 at 4°C to get the crude mitochondria in the pellet. The resulting pellet was resuspended
503 in 10 mL resuspension buffer (50 mM HEPES-KOH pH 7.5, 10 mM KCl, 1.5 mM $MgCl_2$,
504 1 mM EDTA, 1 mM EGTA, 1 mM DTT, 70 mM sucrose, 210 mM mannitol, and 1× protease
505 inhibitor). Genomic DNA was removed by adding of 100 U RNase-free DNase I and
506 centrifugation at 10,000 ×*g* for 15 min at 4 °C. The crude mitochondria were gently
507 resuspended in 1 mL buffer containing 20 mM HEPES-KOH pH 7.5, 1 mM EDTA, 250
508 mM sucrose and loaded onto sucrose gradients comprising 1.5 mL 60% (w/v), 4 mL 32%
509 (w/v), 1.5 mL 23% (w/v) and 1.5 mL 15% (w/v) sucrose solutions in 20mM HEPES-KOH
510 pH 7.5, 1mM EDTA. The gradients were centrifuged at 28,000 rpm for 1h at 4 °C using
511 an SW41Ti rotor (Beckman Coulter). The brown band containing mitochondria migrating
512 to the interface of 32% and 60% sucrose was collected.

513 The fresh isolated mitochondria were resuspended in lysis buffer (25 mM HEPES-KOH
514 pH 7.5, 100 mM KCl, 10 mM $Mg(OAc)_2$, 1.7% Triton X-100, 2 mM DTT, 1× protease
515 inhibitor) at a mitochondria-to-buffer ratio of 1:2 (v/v). The mixture was homogenized with
516 a glass dounce homogenizer. The lysate was cleared by centrifugation at 30,000 ×*g* for
517 20 min at 4 °C. The supernatant was then loaded onto the top of sucrose cushion (1 M
518 sucrose in 20 mM HEPES-KOH pH 7.5, 100 mM KCl, 20 mM $Mg(OAc)_2$, 1% TX-100, 2

519 mM DTT) and centrifuged at 339,200 ×*g* for 45 minutes at 4°C using an MLA130 rotor
520 (Beckman Coulter). The pellet was rinsed and resuspended in Grid buffer (20 mM
521 HEPES-KOH pH 7.5, 100 mM KCl, 10 mM $Mg(OAc)_2$, 0.02% DDM, 1 mM DTT).
522 Mitoribosomes (280 nM) were incubated with 50 μM neomycin (~178-fold excess) for
523 30 min at 4 °C prior to the cryo-EM sample preparation (molar ratio of ribosome to
524 neomycin around 1:170).
525

526 **Human cytosolic ribosome purification**

527 The human cytosolic ribosome was isolated using a modified protocol adapted from a
528 previously published paper[50]. HEK293T cells were harvested at ~80% confluency,
529 centrifuged at 1000 ×*g* for 10 minutes at 4 °C, and washed twice with ice-cold PBS. The
530 cell pellet was resuspended in an equal volume of lysis buffer (10 mM HEPES-KOH pH
531 7.5, 10 mM KOAc, 0.5 mM $Mg(OAc)_2$, 5 mM DTT). Following 20 min incubation on ice,
532 the resuspended cells were mechanically lysed by grinding in a glass homogenizer.
533 Lysates were centrifuged at 1,000 ×*g* for 10 min to remove cell debris, and cleared by
534 centrifugation at 10,000 ×*g* for 15 min at 4 °C. The supernatant was then loaded onto a
535 sucrose cushion (10mM HEPES-KOH pH 7.5, 50mM KCl, 5mM $Mg(OAc)_2$, 0.02% DDM,
536 1mM DTT, 1M sucrose) and centrifuged at 603,000 ×*g* for 45 min at 4 °C in an MLA130
537 Rotor (Beckman Coulter). The pellets obtained were washed and sequentially
538 resuspended in Grid buffer (20 mM HEPES-KOH pH 7.5, 50 mM KCl, 5 mM $Mg(OAc)_2$,
539 0.02% DDM) and measured using an Implen spectrophotometer. Cytosolic ribosomes
540 (294 nM) were incubated with 50 μM neomycin (~170-fold excess) for 30 min at 4 °C prior
541 to the cryo-EM sample preparation (molar ratio of ribosome to neomycin around 1:170).
542

543 **Isolation of mitoribosome and cytosolic ribosome from neomycin treated cells**

544 HEK293F was scaled up sequentially, by inoculating at 1×10^6 cells/mL and subsequently
545 splitting at a cell density of 3.0×10^6 cells/mL until achieving 300 mL final culture volume.
546 Neomycin was added to HEK293F cells to a final concentration of 1 mM for 1 hour prior
547 to utilization. Native human mitoribosomes purification was performed as described for
548 the “Isolation of mitochondria and purification of mitoribosomes” part. And no extra
549 neomycin was added during the purification. The same batch of cells were used for

550 cytosolic ribosome isolation to make strict comparison, meaning we have native
551 mitoribosomes and cytosolic ribosomes from the same cells. After cells harvest and lysis,
552 the supernatant was applied for cytosolic ribosome isolation and the pellet was for crude
553 mitochondria isolation. The protocol for purification of cytosolic ribosomes is the same as
554 described in "Human cytosolic ribosome purification". For the high concentration
555 neomycin treated cells, we treated the cells with 3mM neomycin for 3 h and then
556 conducted the cytosolic ribosomes isolation as described.
557
558 **Cryo-EM grids preparation**
559 The concentration of the mitoribosomes and cytosolic ribosomes used for cryo-EM grid
560 preparation was 280nM and 160 nM. Approximately, 3.2 µL aliquots were applied to a
561 plasma-cleaned holey carbon grid (R1.2/1.3, 300 mesh, Quantfoil) for 1 min, on which a
562 homemade continuous carbon film was precoated. Grids were blotted for 2.5 s under 100%
563 humidity at 4 °C and plunge-frozen in liquid ethane using Vitrobot Mark IV (Thermo Fisher
564 Scientific).
565
566 **Cryo-EM data collection and processing**

567 Cryo-EM micrographs of all samples were collected on a Titan Krios transmission electron
568 microscope (Thermo Fisher Scientific) operated at 300 kV using a slit width of 20 eV on
569 a GIF quantum energy filter (Gatan). The micrographs were recorded using a Falcon 4i
570 direct electron detector at a pixel size of 0.81 Å. A total electron dose of 50 electrons per
571 $Å^2$ was fractionated over 40 frames with a total exposure time of 5.9 s. Data were acquired
572 using EPU software[50] with a defocus ranging from 1.0 to 2.0 µm.

573 All datasets were processed using cryoSPARC v.4.2.1[51]. The movie stacks were first
574 corrected for motion using the patch motion correction tool of cryoSPARC. Contrast
575 transfer function (CTF) parameters were estimated using the patch CTF estimation tool.
576 Manual curation was performed to exclude suboptimal micrographs. From the curated
577 micrographs, particles were initially identified through blob-based template-free picking,
578 followed by iterative template-based particle picking using averaging projections selected
579 from 2D classification. The extracted particles underwent multiple rounds of 2D
580 classification to remove non-ribosomal contaminants and ice artifacts. Particles were then

used for 3D auto-refinement yielding a map for further classification.

Focused 3D classification was carried out using a mask on the SSU to facilitate conformational sorting, enabling separation of rotated versus non-rotated ribosome states. Another round of focused 3D classification using a spherical mask on the tRNA binding sites was performed, separating the particles into different tRNA binding states. H69 and h44 are key binding sites of aminoglycoside antibiotics. Therefore, a spherical mask of radius 23 Å was generated for H69 and h44, respectively, for 3D classification to improve the local resolution. Masks with smoothed edges were generated with the "relion_mask_create" tool in RELION4.0.0[52]. After one round of CTF refinement, particles of each class were further processed by focused refinements with different masks applied. All reported map resolutions were determined by the FSC = 0.143 cutoff criterion.

Model building and refinement

In general, the structures of cytosolic ribosomes (PDB:8QOI[53]) and mitoribosome (PDB: 7QI5[15]) were used for rigid body docking into the cryo-EM density map using UCSF ChimeraX v1.8[54]. The docked coordinates were realigned to match map orientation and saved as models for manual building and adjustment in Coot v0.9.8.1[55]. The neomycin ligand was fetched from the Coot ligand library using the three-letter code: NMY and manually positioned according to the density maps. Conformational changes induced by neomycin binding were also manually adjusted. And the unknown continuous density was analyzed using CryFold[56] to predict the sequence and three-dimensional structure, which was subsequently added into the model. Final models were further subjected to refinement with Phenix.real_space_refine v1.13_2998[57,58]. The figures were prepared with ChimeraX[54]. Figures were compiled using Adobe Illustrator.

Computational methods

mtSSU molecular dynamics (MD) simulations were performed using the AMBER package. The system comprised ribosomal proteins, rRNA, and three neomycin molecules (Neo1, Neo2, Neo3) solvated in an orthorhombic TIP3P water box extending 12 Å beyond the solute. The ff19SB force field was applied to proteins, OL3 to RNA, and GAFF2

610 parameters with AM1-BCC charges to ligands. After energy minimization and stepwise
611 heating, production runs were conducted at 90 K, 280 K, 290 K, 300 K, and 310 K under
612 NPT conditions using a 2-fs timestep with SHAKE constraints. Five independent 100-ns
613 replicates per temperature were acquired. Binding free energies were calculated via the
614 linear interaction energy method using the *cpptraj* module in Ambertools. And the MD of
615 the SSU of the cytosolic ribosome with three neomycin molecules (Neo1, Neo10, and
616 Neo11) were performed as described for the mtSSU.

617

618 **Reporting summary**

619 Further information on research design is available in the Nature Research Reporting
620 Summary linked to this paper.

621

622 **Data availability**

623 The data that support the findings of this study are available from the corresponding
624 authors upon reasonable request. The cryo-EM maps have been deposited in the
625 Electron Microscopy Data Bank under the following accession numbers, respectively:
626 EMD-65426 (*in vitro* dataset, mitoribosomes in non-rotated state with A/A P/P E/E-site
627 tRNA), EMD-65433 (*in vitro* dataset, mitoribosomes in non-rotated state with A/A P/P-site
628 tRNA), EMD-65428 (*in vitro* dataset, mitoribosome in partially rotated state with A/P P/E-
629 site tRNA), EMD-65427 (*in vitro* dataset, mitoribosome in partially rotated state with A/A
630 P/P E/E-site tRNA), EMD-65431 (*in vitro* dataset, mitoribosome in rotated state with A/P
631 P/E-site tRNA), EMD-65429 (*in vitro* dataset, mitoribosome in rotated); EMD-65419 (*in*
632 *vitro* dataset, cytosolic ribosome in non-rotated state with P/P E/E-site tRNA), EMD-65412
633 (*in vitro* dataset, cytosolic ribosome in partially rotated state with eEF2, SERBP1 and E/E-
634 site tRNA), EMD-65434 (*in vitro* dataset, cytosolic ribosome in rotated state with A/P P/E-
635 site tRNA), EMD-65411 (1mM native dataset, cytosolic ribosome in non-rotated state with
636 P/P E/E-site tRNA), EMD-65413 (1mM native dataset, cytosolic ribosome in partially-
637 rotated state with eEF2, SERBP1 and E/E-site tRNA), EMD-65415 (1mM native dataset,
638 cytosolic ribosome in rotated state with A/P P/E-site tRNA), EMD-65414 (1mM native
639 dataset, cytosolic ribosome in rotated state with A/A P/E-site tRNA); EMD-65416 (3mM

640 native dataset, cytosolic ribosome in non-rotated state with P/P E/E-site tRNA), EMD-
641 65417 (3mM native dataset, cytosolic ribosome in partially-rotated state with eEF2,
642 SERBP1 and E/E-site tRNA), EMD-65418 (3mM native dataset, cytosolic ribosome in
643 rotated state with A/P P/E-site tRNA); EMD-65421 (1mM native dataset, mitoribosome in
644 non-rotated state with P/P E/E-site tRNA), EMD-65422 (1mM native dataset,
645 mitoribosome in non-rotated state with A/A P/P E/E-site tRNA), EMD-65423 (1mM native
646 dataset, mitoribosome in partially rotated state with A/A P/P-site tRNA); EMD-65424
647 (native dataset, mitoribosome in partially rotated state with A/P P/E-site tRNA), EMD-
648 65425 (native dataset, mitoribosome in rotated state with P/E-site tRNA), EMD-65420
649 (native dataset, LSU of the mitoribosome). The corresponding atomic coordinates have
650 been deposited in the Protein Data Bank with accession codes 9VXM (mitoribosome in
651 non-rotated state with A/A P/P -site tRNA, corresponding map EMD-65433) and 9VXN
652 (cytosolic ribosome in rotated state with A/P P/E-site tRNA, corresponding map EMD-
653 65434). Source data are provided with this paper.

654

655 **Acknowledgements**

656 We thank Zhengkun Xie from the Center of Advanced Analysis & Gene Sequencing of
657 Zhengzhou University for technical support; Jamie Doudna Cate and Jingdong Cheng for
658 helpful discussions. This work was supported by grants from the National Natural Science
659 Foundation of China (32171291 and 32371351 to W.L., 82302100 to M.W.), National Key
660 Research and Development Program of China (2022YFA0807100 to W.L.,
661 2023YFC2308900 to M.W.), Nature Science Foundation of Shandong Province
662 (ZR2021QC002 to W.L.) the Shandong Excellent Young Scientists Fund Program
663 (2022HWYQ-025), Taishan Scholars Program (tsqnz20221104), Cutting Edge
664 Development Fund of Advanced Medical Research Institute (GYY2023QY01) and the
665 Cheeloo Youth Program of Shandong University to W.L., European Research Council
666 (805230) to A.A..

667

668 **Contributions**

X.Z., L.Z., C.J. and M.W. performed the sample preparation, acquired cryo-EM data, and carried out image processing and structure refinement. L.Z., C.J., W.M. and W.L. did the model building and structural analysis. X.Z., L.Z. and K.W. conducted biochemistry and cell-based experiments. X.H. performed the MD experiment. L.Z., W.L., C.J., W.M. and A.A. prepared the figures. W.L. and A.A. wrote the initial draft of the paper. All authors analyzed the data and edited the paper.

Competing interests

The authors declare no competing interests.

References

1. Kohanski, M. A., Dwyer, D. J. & Collins, J. J. How antibiotics kill bacteria: from targets to networks. *Nat. Rev. Microbiol.* **8**, 423–435 (2010).
2. Lin, J., Zhou, D., Steitz, T. A., Polikanov, Y. S. & Gagnon, M. G. Ribosome-targeting antibiotics: Modes of action, mechanisms of resistance, and implications for drug design. *Annu. Rev. Biochem.* **87**, 451–478 (2018).
3. Paternoga, H. *et al.* Structural conservation of antibiotic interaction with ribosomes. *Nat. Struct. Mol. Biol.* **30**, 1380–1392 (2023).
4. Wilson, D. N. Ribosome-targeting antibiotics and mechanisms of bacterial resistance. *Nat. Rev. Microbiol.* **12**, 35–48 (2014).
5. Becker, B. & Cooper, M. A. Aminoglycoside antibiotics in the 21st century. *ACS Chem. Biol.* **8**, 105–115 (2013).
6. Zaher, H. S. & Green, R. Fidelity at the molecular level: lessons from protein synthesis. *Cell* **136**, 746–762 (2009).
7. Recht, M. I., Douthwaite, S. & Puglisi, J. D. Basis for prokaryotic specificity of action of aminoglycoside antibiotics. *EMBO J.* **18**, 3133–3138 (1999).
8. Moazed, D. & Noller, H. F. Interaction of antibiotics with functional sites in 16S ribosomal RNA. *Nature* **327**, 389–394 (1987).
9. Prezant, T. R. *et al.* Mitochondrial ribosomal RNA mutation associated with both antibiotic-induced and non-syndromic deafness. *Nat. Genet.* **4**, 289–294 (1993).
10. Böttger, E. C., Springer, B., Prammananan, T., Kidan, Y. & Sander, P. Structural basis for selectivity and toxicity of ribosomal antibiotics. *EMBO Rep.* **2**, 318–323 (2001).
11. Hobbie, S. N. *et al.* Genetic analysis of interactions with eukaryotic rRNA identify the mitoribosome as target in aminoglycoside ototoxicity. *Proc. Natl. Acad. Sci. U. S. A.* **105**, 20888–20893 (2008).
12. Guan, M.-X. Mitochondrial 12S rRNA mutations associated with aminoglycoside ototoxicity. *Mitochondrion* **11**, 237–245 (2011).

13. Matt, T. *et al.* Dissociation of antibacterial activity and aminoglycoside ototoxicity in the 4-monosubstituted 2-deoxystreptamine apramycin. *Proc. Natl. Acad. Sci. U. S. A.* **109**, 10984–10989 (2012).
14. Amunts, A., Brown, A., Toots, J., Scheres, S. H. W. & Ramakrishnan, V. Ribosome. The structure of the human mitochondrial ribosome. *Science* **348**, 95–98 (2015).
15. Singh, V. *et al.* Mitoribosome structure with cofactors and modifications reveals mechanism of ligand binding and interactions with L1 stalk. *Nat. Commun.* **15**, 4272 (2024).
16. Fosso, M. Y., Li, Y. & Garneau-Tsodikova, S. New trends in aminoglycosides use. *Medchemcomm* **5**, 1075–1091 (2014).
17. Prokhorova, I. *et al.* Aminoglycoside interactions and impacts on the eukaryotic ribosome. *Proc. Natl. Acad. Sci. U. S. A.* **114**, E10899–E10908 (2017).
18. Palmer, E., Wilhelm, J. M. & Sherman, F. Phenotypic suppression of nonsense mutants in yeast by aminoglycoside antibiotics. *Nature* **277**, 148–150 (1979).
19. Manuvakhova, M., Keeling, K. & Bedwell, D. M. Aminoglycoside antibiotics mediate context-dependent suppression of termination codons in a mammalian translation system. *RNA* **6**, 1044–1055 (2000).
20. Keeling, K. M., Xue, X., Gunn, G. & Bedwell, D. M. Therapeutics based on stop codon readthrough. *Annu. Rev. Genomics Hum. Genet.* **15**, 371–394 (2014).
21. Shalev, M. *et al.* Structural basis for selective targeting of leishmanial ribosomes: aminoglycoside derivatives as promising therapeutics. *Nucleic Acids Res.* **43**, 8601–8613 (2015).
22. Sabbavarapu, N. M. *et al.* Design of novel aminoglycoside derivatives with enhanced suppression of diseases-causing nonsense mutations. *ACS Med. Chem. Lett.* **7**, 418–423 (2016).
23. Benveniste, R. & Davies, J. Structure-activity relationships among the aminoglycoside antibiotics: role of hydroxyl and amino groups. *Antimicrob. Agents Chemother.* **4**, 402–409 (1973).
24. Wang, L. *et al.* Allosteric control of the ribosome by small-molecule antibiotics. *Nat. Struct. Mol. Biol.* **19**, 957–963 (2012).
25. Wallis, M. G., von Ahsen, U., Schroeder, R. & Famulok, M. A novel RNA motif for neomycin recognition. *Chem. Biol.* **2**, 543–552 (1995).
26. Borovinskaya, M. A. *et al.* Structural basis for aminoglycoside inhibition of bacterial ribosome recycling. *Nat. Struct. Mol. Biol.* **14**, 727–732 (2007).
27. Wasserman, M. R. *et al.* Chemically related 4,5-linked aminoglycoside antibiotics drive subunit rotation in opposite directions. *Nat. Commun.* **6**, 7896 (2015).
28. Fourmy, D., Recht, M. I., Blanchard, S. C. & Puglisi, J. D. Structure of the A site of Escherichia coli 16S ribosomal RNA complexed with an aminoglycoside antibiotic. *Science* **274**, 1367–1371 (1996).
29. Smolkin, B. *et al.* Towards catalytic antibiotics: Redesign of aminoglycosides to catalytically disable bacterial ribosomes. *Chembiochem* **20**, 247–259 (2019).
30. Chen, B. *et al.* PGC-1α-mediated imbalance of mitochondria-lipid droplet homeostasis in neomycin-induced ototoxicity and nephrotoxicity. *Acta Pharm. Sin. B.* **14**, 4413–4430 (2024).
31. Itoh, Y. *et al.* Structure of the mitoribosomal small subunit with streptomycin reveals Fe-S clusters and physiological molecules. *Elife* **11**, (2022).

753 32. Sighel, D. *et al.* Inhibition of mitochondrial translation suppresses glioblastoma stem
754 cell growth. *Cell Rep.* **35**, 109024 (2021).
755 33. Aibara, S., Andréll, J., Singh, V. & Amunts, A. Rapid isolation of the mitoribosome
756 from HEK cells. *J. Vis. Exp.* (2018) doi:10.3791/57877.
757 34. Carter, A. P. *et al.* Functional insights from the structure of the 30S ribosomal subunit
758 and its interactions with antibiotics. *Nature* **407**, 340–348 (2000).
759 35. Holm, M. *et al.* mRNA decoding in human is kinetically and structurally distinct from
760 bacteria. *Nature* **617**, 200–207 (2023).
761 36. Ogle, J. M. *et al.* Recognition of cognate transfer RNA by the 30S ribosomal subunit.
762 *Science* **292**, 897–902 (2001).
763 37. An, H., Ordureau, A., Körner, M., Paulo, J. A. & Harper, J. W. Systematic quantitative
764 analysis of ribosome inventory during nutrient stress. *Nature* **583**, 303–309 (2020).
765 38. Yousefi, R. *et al.* Monitoring mitochondrial translation in living cells. *EMBO Rep.* **22**,
766 e51635 (2021).
767 39. Li, X. *et al.* Structural basis for differential inhibition of eukaryotic ribosomes by
768 tigecycline. *Nat. Commun.* **15**, 5481 (2024).
769 40. Rosenberg, C. R., Fang, X. & Allison, K. R. Potentiating aminoglycoside antibiotics
770 to reduce their toxic side effects. *PLoS One* **15**, e0237948 (2020).
771 41. Le, T. A. *et al.* Aminoglycoside-related nephrotoxicity and ototoxicity in clinical
772 practice: A review of pathophysiological mechanism and treatment options. *Adv.*
773 *Ther.* **40**, 1357–1365 (2023).
774 42. Aibara, S., Singh, V., Modelska, A. & Amunts, A. Structural basis of mitochondrial
775 translation. *Elife* **9**, (2020).
776 43. Itoh, Y. *et al.* Mechanism of membrane-tethered mitochondrial protein synthesis.
777 *Science* **371**, 846–849 (2021).
778 44. Bock, L. V. & Grubmüller, H. Effects of cryo-EM cooling on structural ensembles. *Nat.*
779 *Commun.* **13**, 1709 (2022).
780 45. Hammill, T. L. & Campbell, K. C. Protection for medication-induced hearing loss: the
781 state of the science. *Int. J. Audiol.* **57**, S67–S75 (2018).
782 46. Garetz, S. L., Altschuler, R. A. & Schacht, J. Attenuation of gentamicin ototoxicity by
783 glutathione in the guinea pig in vivo. *Hear. Res.* **77**, 81–87 (1994).
784 47. Li, W., Chang, S. T.-L., Ward, F. R. & Cate, J. H. D. Selective inhibition of human
785 translation termination by a drug-like compound. *Nat. Commun.* **11**, 4941 (2020).
786 48. Li, W. *et al.* Structural basis for selective stalling of human ribosome nascent chain
787 complexes by a drug-like molecule. *Nat. Struct. Mol. Biol.* **26**, 501–509 (2019).
788 49. Lintner, N. G. *et al.* Selective stalling of human translation through small-molecule
789 engagement of the ribosome nascent chain. *PLoS Biol.* **15**, e2001882 (2017).
790 50. Thompson, R. F., Iadanza, M. G., Hesketh, E. L., Rawson, S. & Ranson, N. A.
791 Collection, pre-processing and on-the-fly analysis of data for high-resolution, single-
792 particle cryo-electron microscopy. *Nat. Protoc.* **14**, 100–118 (2019).
793 51. Punjani, A., Rubinstein, J. L., Fleet, D. J. & Brubaker, M. A. cryoSPARC: algorithms
794 for rapid unsupervised cryo-EM structure determination. *Nat. Methods* **14**, 290–296
795 (2017).
796 52. Kimanius, D., Dong, L., Sharov, G., Nakane, T. & Scheres, S. H. W. New tools for
797 automated cryo-EM single-particle analysis in RELION-4.0. *Biochem. J.* **478**, 4169–
798 4185 (2021).

53. Holvec, S. *et al.* The structure of the human 80S ribosome at 1.9 Å resolution reveals the molecular role of chemical modifications and ions in RNA. *Nat. Struct. Mol. Biol.* **31**, 1251–1264 (2024).
54. Goddard, T. D. *et al.* UCSF ChimeraX: Meeting modern challenges in visualization and analysis. *Protein Sci.* **27**, 14–25 (2018).
55. Emsley, P., Lohkamp, B., Scott, W. G. & Cowtan, K. Features and development of coot. *Acta Crystallogr. D Biol. Crystallogr.* **66**, 486–501 (2010).
56. Su, B., Huang, K., Peng, Z., Amunts, A. & Yang, J. Improved automated model building for cryo-EM maps using CryFold. *bioRxiv* (2024) doi:10.1101/2024.11.13.623164.
57. Afonine, P. V. *et al.* Real-space refinement in PHENIX for cryo-EM and crystallography. *Acta Crystallogr. D Struct. Biol.* **74**, 531–544 (2018).
58. Liebschner, D. *et al.* Macromolecular structure determination using X-rays, neutrons and electrons: recent developments in Phenix. *Acta Crystallogr. D Struct. Biol.* **75**, 861–877 (2019).